ac electric trapping of neutral atoms

Sophie Schlunk,[1,2,*] Adela Marian,[1] Wieland Schöllkopf,[1] and Gerard Meijer[1]
[1]*Fritz-Haber-Institut der Max-Planck-Gesellschaft, Faradayweg 4-6, 14195 Berlin, Germany*
[2]*FOM-Institute for Plasmaphysics Rijnhuizen, P. O. Box 1207, 3430 BE Nieuwegein, The Netherlands*
(Received 21 January 2008; published 11 April 2008)

We study the dynamic behavior of ultracold neutral atoms in a macroscopic ac electric trap. Confinement in such a trap is achieved by switching between two saddle-point configurations of the electric field. The gradual formation of a stably trapped cloud is observed and the trap performance is studied versus the switching frequency and the symmetry of the switching cycle. Additionally, the electric field in the trap is mapped out by imaging the atom cloud while the fields are still on. Finally, the phase-space acceptance of the trap is probed by introducing a modified switching cycle. The experimental results are reproduced using full three-dimensional trajectory calculations.

DOI: 10.1103/PhysRevA.77.043408 PACS number(s): 37.10.Gh, 32.60.+i, 37.10.−x

I. INTRODUCTION

The trapping of neutral particles has paved the way for remarkable achievements in atomic and molecular physics, culminating with the observation of degenerate Bose and Fermi gases [1,2]. The ability to confine the ground state of neutral particles is becoming important for an increasing number of experiments, in particular for collision studies [3]. The ground state of any neutral particle is always attracted toward a point of maximum field, but it cannot be trapped in a static field, as static fields cannot possess a maximum in free space [4,5]. Trapping in the ground state is therefore only possible when electrodynamic fields are used. For example, any sublevel of the ground state can be confined in the laser field maximum of a dipole trap [6], which has been successfully demonstrated for both atoms [7] and molecules [8]. Additionally, paramagnetic particles can be trapped using ac magnetic fields, as shown for ground-state Cs atoms [9].

Trapping by ac electric fields is a more versatile method, applicable to any ground-state atom or molecule. For polar molecules strong confinement can be achieved via the first-order Stark interaction. For atoms and nonpolar molecules, trapping is based on the second-order Stark interaction between an external electric field and the induced dipole moment. Similarly to trapping of ions in a Paul trap [10], three-dimensional confinement in an ac electric trap is achieved by alternating between two saddle-point configurations of the electric field. The first configuration has attractive (focusing) forces along one direction and repulsive (defocusing) forces along the other two directions, while in the second configuration the roles of the forces are reversed. Dynamic confinement of the particles is obtained by switching between these two configurations at the appropriate frequency.

The first demonstration of ac electric trapping was carried out for ammonia molecules using a cylindrically symmetric trap with a depth of several millikelvins [11]. Similar trap depths were later obtained for the same molecule with a linear ac trap [12]. In the meantime, Katori and co-workers achieved trapping of about 100 ground-state Sr atoms with a lifetime of 80 ms in a microstructured ac trap on a chip [13]. Recently, we demonstrated trapping of about 10^5 Rb atoms in a 1 mm^3 large and several microkelvins deep trap, with a lifetime of about 5 s [14]. Our trap is also based on the cylindrically symmetric geometry suggested by Peik [15]. It allowed for the first direct visualization of the dynamic confinement in an ac trap using absorption images taken at different phases of the ac switching cycle. Subsequently, trapping of ultracold Rb atoms was also obtained with a three-phase ac electric trap [16], as proposed by Shimizu and Morinaga [17,18]. A recent paper describes in detail the ac trap geometries currently used to electrically confine neutral atoms and molecules [19].

In this paper, we present a detailed experimental investigation of the dynamics in the ac trap and study the dependence of the atom number on the switching-cycle parameters. Compared to our previous measurements [14], we have optimized the number of trapped atoms by introducing an evaporative cooling stage before loading the atoms into the ac trap. As the depth of the ac trap is small, the reduction in temperature helped increase the number of confined particles, which in turn improved the quality of our images. The experimental data are compared throughout the paper with results of numerical simulations based on classical trajectory calculations.

This paper is organized as follows. We start by describing the experimental sequence used to load the atoms into the ac trap in Sec. II. The ac trap is presented in detail in Sec. III and the theory model we use for the simulations is also briefly discussed. Next, we show how the atoms can be used to probe the electric fields in the trap in Sec. IV. The formation of a trapped cloud in the ac trap is studied in Sec. V by imaging the atoms after a gradually increasing number of switching cycles. This also leads to a measurement of the ac trap lifetime. Then, in Sec. VI, the dynamics of the atoms in the ac trap is visualized at different phases of the ac switching cycle. Additionally, the dependence of the trapped atom number on the trapping frequency and the symmetry of the switching cycle is measured. Furthermore, the mean kinetic energy of the atoms is determined at different phases of the switching cycle. In Sec. VII we study the phase-space acceptance of the ac trap by introducing a sudden change in the

*schlunk@fhi-berlin.mpg.de

switching cycle. Finally, we summarize our results in Sec. VIII.

II. EXPERIMENTAL PROCEDURE

In the experiment, the ^{87}Rb atoms are first collected in a six-beam magneto-optical trap (MOT) loaded from a Zeeman slower. After a short compression of the MOT, optical molasses cooling, and optical pumping, the atoms are transferred into a spatially overlapped quadrupole magnetic trap. About 5×10^8 atoms in the $F=2$, $m_F=2$ hyperfine sublevel at a temperature of 600 μK are trapped in the magnetic trap, which is characterized by a field gradient of 270 G/cm along its symmetry axis. A short evaporative cooling stage is applied next by linearly ramping a radio frequency from 35 to 6 MHz in 8.3 s. At the end of the evaporative cooling stage, the field gradient is reduced to 65 G/cm. Approximately 2×10^7 atoms remain magnetically trapped at a temperature of 30 μK. The quadrupole magnet is then moved horizontally in 3 s to a second quartz cell located 42 cm away [20]. This second ultrahigh-vacuum chamber houses the ac trap. The transfer is carried out using a precision translation stage allowing for accurate overlap of the cloud with the center of the ac trap. Altogether, the cooling, trapping, and transport of the atoms take about 25 s. At the final position, the magnetic field is switched off and, once it has completely disappeared, high voltage is applied to the ac trap electrodes. After a variable trapping time, the trap electrodes are switched back to ground and the confined atoms are detected by absorption imaging. In a typical experiment, the atoms are imaged 0.1 ms after the high voltage has been turned off, thereby reflecting the spatial distribution at the time of switch-off. The number of atoms is determined with an accuracy of about 5% using a two-dimensional Gaussian fitting procedure.

III. TRAP DESIGN

In the following, we give a description of the ac trap and briefly introduce our model for theory simulations.

The ac trap consists of two end cap electrodes and two ring electrodes as shown in Fig. 1. The inset is a schematic cross section of the cylindrically symmetric trap, while the photograph zooms in on the trap used in the experiment. The four electrodes are made of nonmagnetic stainless steel and are mounted between two macor plates using macor spacers. The two ring electrodes are located between the end caps, but the ring opening is not visible in the photograph because the picture is taken from the side. As indicated in the schematic, the end caps have a hemispherical shape with a diameter of 7 mm and are separated by 6 mm. The ring electrodes are 3 mm thick, corresponding to an inner semicircular shape with a radius of 1.5 mm. They have an opening diameter of 6.7 mm and are separated by a 2 mm gap. All electrodes were highly polished before the trap was assembled and were subsequently conditioned to withstand increasingly high voltages.

A superposition of a static dipole field and an alternating hexapole field is used to switch between the two saddle-point configurations [15]. Because only the hexapole field is switched, the field strength remains constant at the center of the trap. Additionally, a dc quadrupole field is applied to counteract gravity. The two saddle-point configurations are referred to as ρ and z focusing. To alternate between these two configurations, two different voltage sets are applied to the four electrodes, as indicated in the photograph in Fig. 1. The ac switching frequency is given by $1/T$, where T is the sum of the durations of the ρ-focusing and z-focusing phases, i.e., the duration of one full switching cycle.

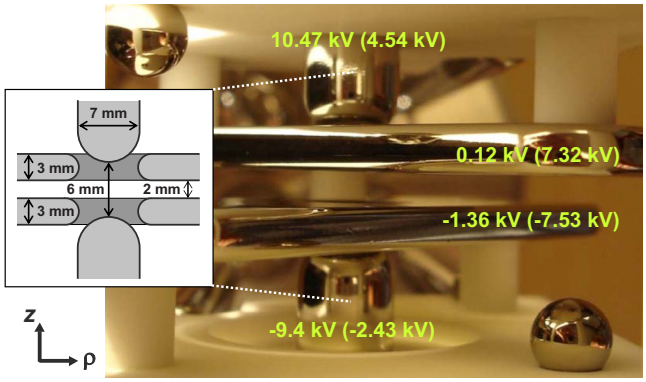

FIG. 1. (Color online) Photograph of the ac trap. The inset on the left shows a schematic of the trap where the dimensions of the electrodes and the distances between them are indicated. The voltages applied to the electrodes during the ρ-focusing (z-focusing) phase are written on each electrode.

The calculated fields that the atoms experience in the two different switching configurations are plotted in Figs. 2(a) and 2(b). For the ρ-focusing configuration in Fig. 2(a), the field has a maximum in ρ and a minimum in z, and the highest field value is found at the top of the picture. For z focusing the situation is reversed; the field has the maximum in z and the highest fields are positioned symmetrically on the left and right sides of the picture. Note that the saddle points are displaced in z due to the dc quadrupole field used for gravity compensation. The z-direction gradients for this field have the same value for both trapping configurations.

To describe the fields in the trap, we approximate the electric potential by a multipole expansion. Taking the cylindrical symmetry into account, the first five terms read

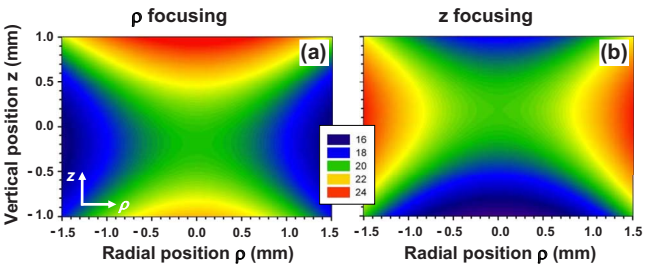

FIG. 2. (Color online) Calculated electric field (in kV/cm) in the trap for the ρ-focusing (a) and z-focusing (b) configurations.

$$\Phi(\rho,r) = \Phi_0 + \Phi_1\frac{z}{z_0} + \Phi_2\frac{z^2-\rho^2/2}{z_0^2} + \Phi_3\frac{z^3-\frac{3}{2}z\rho^2}{z_0^3} + \Phi_4\frac{z^4-3\rho^2z^2+\frac{3}{8}\rho^4}{z_0^4} + \Phi_5\frac{z^5-5z^3\rho^2+\frac{15}{8}z\rho^4}{z_0^5}, \quad (1)$$

where $2z_0=6$ mm is the distance between the end cap electrodes and the Φ_i characterize the different multipole terms. The first term describes a constant potential, the second term represents a dipole field, the Φ_2 term is the quadrupole potential, and the Φ_3 term is the hexapole component. The Φ_4 and Φ_5 terms are octupolar and decapolar field components. These last two higher-order terms represent undesirable nonlinearities in the system.

Simulations are carried out to model the experimental results. First, the electric fields for our trap geometry are calculated using a commercial finite-element program (COMSOL). A multipole series up to the fifth term as shown in Eq. (1) is then fitted to these fields. For the trap geometry presented in Fig. 1, the multipole term components are $\Phi_0=-285$ V, $\Phi_1=5992$ V, $\Phi_2=604$ V, $\Phi_3=3265$ V, $\Phi_4=222$ V, and $\Phi_5=737$ V for ρ focusing, and $\Phi_0=232$ V, $\Phi_1=5991$ V, $\Phi_2=607$ V, $\Phi_3=-3263$ V, $\Phi_4=223$ V, and $\Phi_5=687$ V for z focusing. The forces acting on the atoms are then derived and trajectory calculations are carried out by numerically integrating the equations of motion. A fine grid in phase space is used to simulate the initial distribution of atoms. Throughout the paper, simulation results will be presented in conjunction with experimental data.

IV. MAPPING OF THE ELECTRIC FIELDS

We will now describe how the atoms can be used to sensitively probe the actual electric fields in the trap. This is important because small inaccuracies and misalignments of the electrodes can have a strong impact on the trapping fields.

To probe the electric fields in the ac trap, the usual experimental sequence is followed with the only exception that the electric fields are kept on while taking absorption images of the cloud. The atoms are confined in the ac trap for a short trapping time during the first switching cycle and the electrodes are switched to ground after obtaining the absorption images. To compensate for the resulting Stark shift, the absorption beam is detuned by several megahertz while the atoms are probed. We have already seen in Fig. 2 that the electric field strength varies significantly over the size of the atom cloud. Therefore, the position of an atom determines whether it is on resonance with the probing transition. Note that the absorption beam crosses the entire cloud and due to the cylindrical symmetry it can be thought of as passing once from left to right through the fields shown in the contour plots in Fig. 2.

In the electronic $5\,^2S_{1/2}$ $(F=2)$ ground state, the m_F sublevels remain degenerate in an electric field. In the $5\,^2P_{3/2}$ $(F=3)$ excited state, however, the degeneracy is lifted due to the tensor polarizability [21], as seen in the inset of Fig. 3. This gives rise to four possible energy differences (Stark shifts) between the two states, which are plotted in Fig. 3.

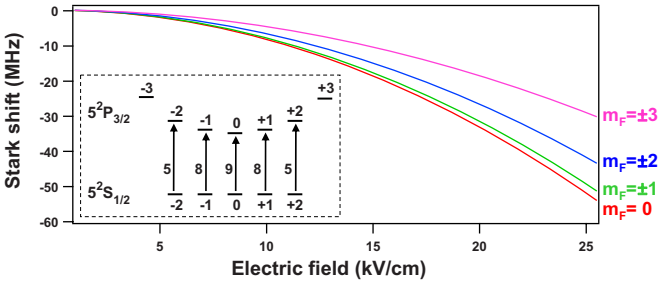

FIG. 3. (Color online) Stark shift of the $5\,^2S_{1/2}$ $(F=2)$ $\rightarrow 5\,^2P_{3/2}$ $(F=3)$ transition used for probing. For the upper state the Stark shift is different for the $|m_F|$ sublevels, while for the lower state all m_F sublevels are degenerate. This can also be seen in the inset which shows the probing transition. All degenerate sublevels of the $5\,^2S_{1/2}$ $(F=2)$ state are populated in the trap; the linearly polarized probe beam drives only transitions with $\Delta m_F=0$. The relative transition strengths are indicated next to the arrows.

In Fig. 4 the first two columns show images of the atoms in the ρ-focusing and z-focusing configurations, respectively. The third and fourth columns display simulation results. For the ρ-focusing pictures in the first column, the atoms are trapped for 9.83 ms, just before switching to z focusing. For the measurements shown in the second column, the atoms are imaged immediately after switching to the z-focusing

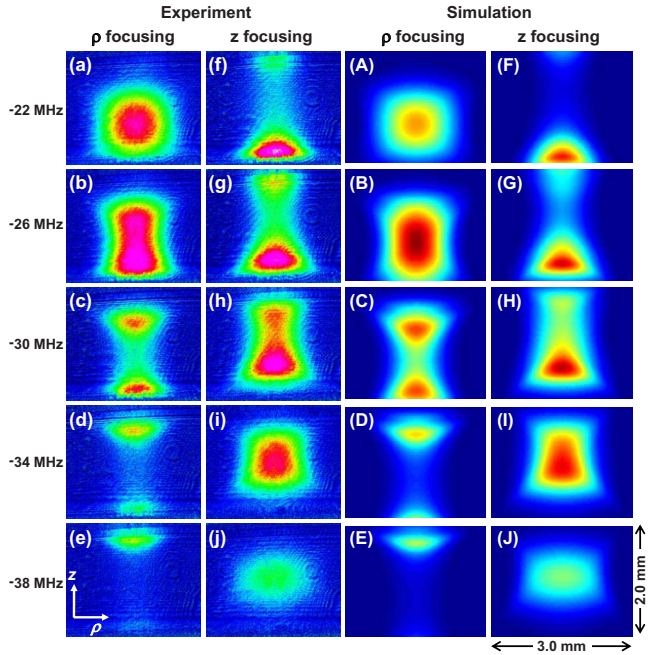

FIG. 4. (Color online) Absorption images (a)–(j) and simulations (A)–(J) of the atom cloud for different probe detunings with the electric fields still on. The first column displays images recorded during ρ focusing, when the atoms are kept in the trap for 9.83 ms. For the second column, the atoms are probed in the z-focusing configuration after a trapping time of 9.84 ms. All absorption images are averaged five times. The pictures in the third and fourth columns show the corresponding simulations.

configuration, namely, after a trapping time of 9.84 ms. The difference in trapping times for the two configurations is tiny and ensures that the atom density distributions are identical. Additionally, for these short trapping times the atom cloud is dense, resulting in a good absorption signal. The experiment is repeated, varying the probe detuning from −22 to −38 MHz. Depending on the detuning, different electric field regions are visible, thus enabling direct probing of the field distributions shown in Fig. 2. For instance, the atom distributions in Figs. 4(c) and 4(g) look like an hourglass, thereby resembling the shapes of the fields in Fig. 2, with the saddle points located at the waist of the hourglass. As expected, the waists are displaced in z for the two pictures. The simulations, labeled with matching capital letters, agree well with the measurements.

Looking at the pictures in the first column, the lower fields corresponding to a small probe detuning are found in the center [Fig. 4(a)]. The higher fields at the top and at the bottom become visible for the larger detunings of −34 MHz in Fig. 4(d) and −38 MHz in Fig. 4(e). Note that the field strength is higher at the top than at the bottom, in agreement with Fig. 2(a). The trend is reversed for the z-focusing configuration shown in the second column. For a small detuning of −22 MHz [Fig. 4(f)], atoms at the top and at the bottom are on resonance. With increasing detuning only atoms at the center of the trap are visible, confirming that along the z axis the highest fields are in the center of the trap as seen in Fig. 2(b). Additionally, in the case of z focusing, the higher fields toward larger ρ play a role. Nonetheless, the highest fields on the left and on the right side of the trap are not visible because the atom cloud is more dilute at larger ρ, and therefore the atom density is too low to image these trap regions.

As mentioned in Sec. III, our simulations are carried out using a finite-element program to determine the electric field in the trap. The probe beam attenuation by an atom cloud with a Gaussian density distribution is calculated for the simulated electric fields. The resulting theory plots are shown in Figs. 4(A)–4(J). In the magnetic trap only the $m_F=+2$ sublevel of the $5\ ^2S_{1/2}$ $(F=2)$ state is populated, while in the electric trap there no longer is a preferred orientation axis and the atoms redistribute over the degenerate m_F sublevels. However, the dipole component of the electric field is dominant at the trap center, and therefore the field points downward along the z axis across the whole imaging region. The probe beam is linearly polarized with its polarization vector almost parallel to this axis. In general, if linearly polarized light is aligned with the quantization axis, there are no circular polarization components. Therefore, the probe beam drives only transitions with $\Delta m_F=0$, as indicated in the inset in Fig. 3. Hence, no transitions to the $m_F=\pm 3$ levels of the upper $5\ ^2P_{3/2}$ $(F=3)$ state are possible. The strength of the allowed transitions varies as shown in the inset in Fig. 3 and is accounted for in the simulations by weighting the transitions accordingly. The natural linewidth of the transition is 6 MHz; therefore the beam can simultaneously excite transitions with different m_F, if the upper sublevels are close enough in frequency. The linewidth of the laser is in the submegahertz regime and thus has a negligible contribution.

From the simulations we determine that the actual fields in the ρ-focusing configuration are lower than expected for the ideal geometry presented in Fig. 1. In contrast, the simulations for z focusing match well. These lower electric fields can be reproduced by moving the lower end cap electrode down by 0.25 mm in the simulations. The calculations with the retracted end cap electrode are shown in Fig. 4 and they agree remarkably well with the corresponding experimental images for both trapping configurations. The displacement of the end cap results in considerable changes only for the ρ-focusing fields. In the z-focusing configuration, it is the ring electrodes that are primarily important for creating the maximum along z, whereas the end cap voltages are relatively low.

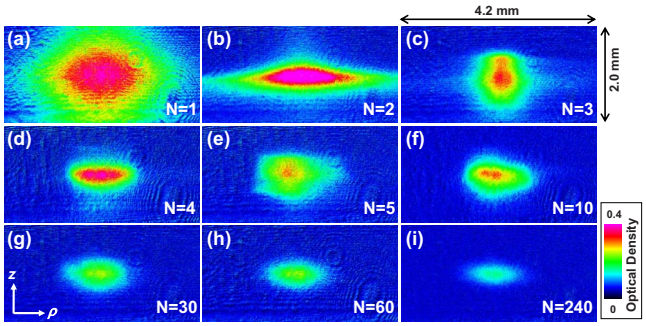

FIG. 5. (Color online) Gradual formation of the trapped atom cloud. The pictures are taken at a switching frequency of 60 Hz and show the cloud after $N=1$, 2, 3, 4, 5, 10, 30, 60, and 240 full switching cycles. All images are averaged five times. The corresponding optical density is indicated by the color scale.

By comparing the simulations with the measurements, we conclude that in-trap imaging of the atoms is a very convenient method to monitor the electric fields in the trap. Using the simulations we are able to verify the geometry of our trap and determine possible inaccuracies. All further simulations discussed in the paper are carried out using the fields associated with the retracted end cap geometry.

V. FORMATION OF THE TRAPPED CLOUD

We will now examine the onset of stable ac electric trapping by imaging cloud shapes after a small number of switching cycles. Figure 5 shows the gradual formation of a trapped cloud as an increasing number N of full switching cycles is applied. The absorption images always show the 2 mm gap between the ring electrodes. In Fig. 5(a) only one switching cycle at 60 Hz has been employed and the atoms completely fill the space available to them. Note that without application of this switching cycle the atoms would have by now fallen out of view due to gravity. After $N=2$ switching cycles, as displayed in Fig. 5(b), the shape of the cloud has changed dramatically. Compared to Fig. 5(a), the number of atoms is now much smaller and the cloud is almost pancake shaped. In Fig. 5(c) after $N=3$ switching cycles, the cloud has taken a rounder shape. The "final" shape emerges only after $N=4$ switching cycles, as can be seen in Figs. 5(d) and 5(e). However, most of the atoms are still metastably trapped and will finally escape from the trap. After $N=5$ and $N=10$ switching cycles, the cloud exhibits an asymmetric shape, which is visible in Figs. 5(e) and 5(f), respectively. This

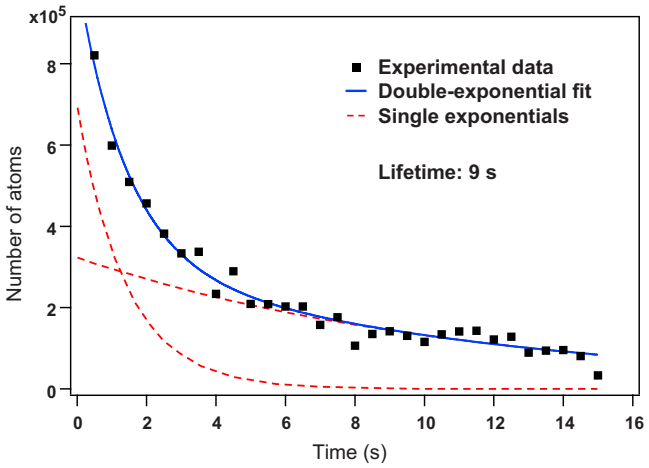

FIG. 6. (Color online) Lifetime measurement of the ac trapped atom cloud. The experiment is performed at 60 Hz, and all the data points are single-shot measurements. The solid line is a double-exponential fit to the data points, while the dashed curves show each exponential individually.

asymmetry can be attributed to possible misalignments between the center of the magnetic trap and the center of the ac trap. Even after $N=30$ switching cycles [Fig. 5(g)] the shape is not as smooth as in Fig. 5(h) after $N=60$ switching cycles. A small feature is still visible on the left side of the cloud. However, the shape remains unchanged at longer trapping times, as illustrated in Fig. 5(i) where the number of atoms has decreased due to collisions with the background gas.

We also studied the atom loss from the trap more quantitatively by recording the number of atoms in the first 0.5 s of trapping. The fast decrease during the first ten switching cycles observed in the images can be fitted by an exponential yielding a $1/e$ lifetime of about 100 ms. This can be attributed to the fact that most of the metastably trapped atoms leave the trap region within the first few switching cycles.

Figure 6 illustrates the lifetime in the ac trap, which is limited by the collisions with the background gas. Displayed is the number of atoms versus the trapping time in seconds. We image the atom cloud at trapping times of up to 15 s, which corresponds to $N=900$ switching cycles at the switching frequency of 60 Hz. The data points are fit using a double exponential yielding a value of 9 s for the lifetime and a value of 1 s for the fast decay. Similarly to the 100 ms decay in the previous paragraph, this fast decay accounts for metastably trapped atoms. These atoms, however, survive in the trap much longer, as they almost have the correct initial conditions to be stably trapped. The 9 s lifetime value is consistent with measurements of a magnetically trapped cloud, performed in the same vacuum chamber.

We therefore conclude that at least 60 switching cycles have to be used in the experiment. Otherwise, the dynamics would be mainly guided by the behavior of metastably trapped atoms. Imaging the atoms after a trapping time of 1 s is a good compromise between stable behavior of the atoms and good signals, as longer trapping times suffer from atom loss due to background collisions.

VI. TRAP PERFORMANCE

In this section, we first visualize the dynamic confinement of the atoms in the trap by looking at the atomic distribution at different times within a switching cycle. From this we can qualitatively understand the motion in the trap. Next, we study the dependence of the number of trapped atoms on the switching frequency. Finally, we analyze the asymmetry of the switching cycle and present measurements on the mean kinetic energy of the atoms.

Characteristic for an ac trap is the fact that trapping is dynamic, i.e., the atoms are forced to move during the switching cycle, which is referred to as micromotion in ion traps. This can be seen in Fig. 7 where the images on the left show the atom cloud at different phases within the 61st switching cycle for a trapping frequency of 60 Hz. The corresponding phases A–D are indicated on the switching cycle, which is asymmetric with 59% of ρ focusing followed by 41% of z focusing.

In Fig. 7(a) the atoms have just experienced z focusing and they are therefore moving inward along z and outward along ρ. Consequently, in the middle of ρ focusing, the cloud is focused in z and elongated in ρ, as shown in Fig. 7(b). However, the ρ-focusing forces have decelerated the motion along both axes and the atoms are now at the turning point of the micromotion before they change direction. Due to this

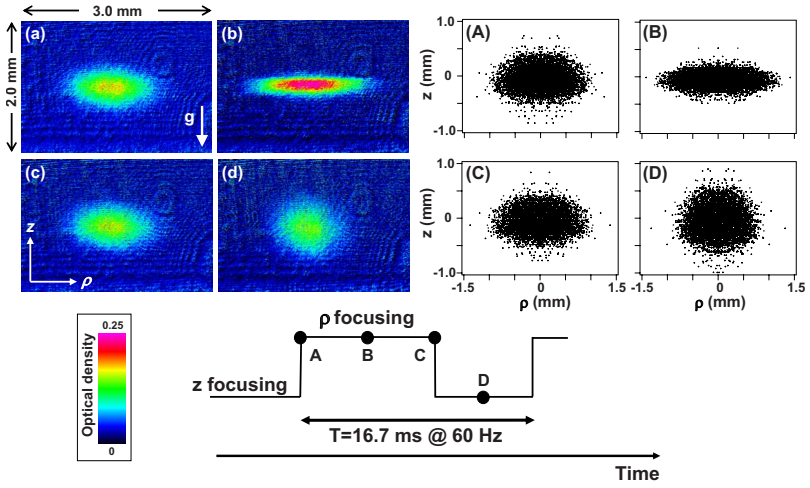

FIG. 7. (Color online) Absorption images (a)-(d) of the atom cloud at different phases within the 61st switching cycle at a trapping frequency of 60 Hz. The pictures (A)–(D) are simulation results of the atomic distribution, labeled with matching capital letters. The schematic shows the applied switching cycle, where the appropriate phases are also indicated. The measurements are averaged five times, and the optical density is shown in the color scale.

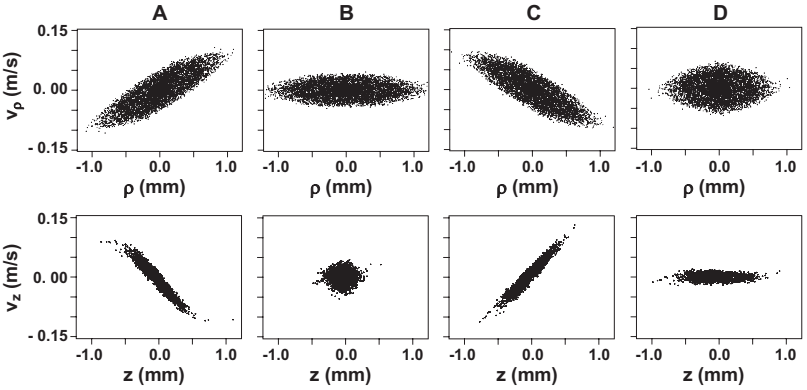

FIG. 8. Radial (first row) and axial (second row) simulated phase-space distributions of the atoms at different trap phases during the 61st switching cycle. The phase space plots are obtained for the same switch-off times A–D used in Fig. 7, as indicated for each column. Note that for the simulations in ρ a finer grid is used for small velocities and small positions, thus increasing the density of particles around zero.

motion, inward in ρ and outward in z, the cloud in Fig. 7(c) has a shape similar to that in Fig. 7(a). But as the atoms have just experienced the ρ-focusing phase, the velocity components are now pointing toward the center of the trap in ρ and outward in z. This leads to a contraction in ρ as shown in Fig. 7(d), which is recorded in the middle of z focusing where the cloud shape is round. As in Fig. 7(b), the atoms are at a standstill before they turn around. At the end of the switching cycle the cloud shape will be identical to the one in Fig. 7(a). Figures 7(A)–7(D) show simulations of the atomic distribution at the same switching times within the 61st cycle as the experimental data Figs. 7(a)–7(d). The agreement between the simulations and the experimental data is very good.

Figure 8 illustrates the evolution of the phase-space distributions during the 61st switching cycle. The radial velocity v_ρ is plotted versus ρ in the first row, and the axial velocity v_z is plotted versus z in the second row. These plots result from the same simulations carried out for the position distributions in Figs. 7(A)–7(D) and show the corresponding radial and axial phase-space distributions. The capital letters indicate for each column the appropriate switch-off time. For the simulations in ρ, a finer grid is used for the values around zero in order to eliminate possible numerical inaccuracies.

For both coordinates ρ and z, the distribution is oscillating in both position and velocity. For the pictures in the first row, the distribution is rotating clockwise from A via B to C; for the second row the same happens from C via D to A. The velocity spread is maximal for A and C where the distribution is tilted by 45°. Some particles are moving at a speed of more than 0.1 m/s, which corresponds to a temperature of about 50 μK. Note that the spread in ρ and v_ρ is larger than the spread in z and v_z. As mentioned before, the atoms are at the turning point of the micromotion when they are in the middle of the focusing (defocusing) stage. The spread in position is maximal in the middle of the focusing stage, i.e., along ρ in B and along z in D, as also seen in the corresponding pictures in Fig. 7. On the other hand, the velocity spread is always minimal at these points, i.e., for v_ρ in B and for v_z in D. In the middle of defocusing, the cloud shape becomes round, as seen for ρ in D and for z in B. Note that the phase space distributions shown are equivalent to the phase space acceptance of the trap at that particular moment in the switching cycle. These phase space distributions have been analyzed in detail for the case of molecules moving in the same trapping configuration [19].

To characterize the mean kinetic energy of the cloud, we perform ballistic expansion measurements of the trapped atoms. These time-of-flight (TOF) measurements are carried out at various trap phases within the 61st switching cycle at our standard switching frequency of 60 Hz. Figure 9(a) shows a typical TOF series where the cloud is imaged after a trapping time of 1016 ms, i.e., toward the end of the z-focusing phase. Plotted is the measured full width at half maximum (FWHM) of the cloud versus the TOF. The kinetic energy is determined from a fit to the measured FWHM, where the initial density and velocity distributions are assumed to be Gaussian. The fit yields a value of $E_\rho = k_B \times 38$ μK in the radial direction (squares), and a value of $E_z = k_B \times 10$ μK in the axial direction (circles) where k_B is the Boltzmann constant. Note that the size of the cloud in the axial direction first decreases to a minimum value at 5 ms, because the atoms are moving toward the center at this particular switch-off time. Then, the cloud FWHM increases as the atoms continue to move along z and the cloud spreads out, i.e., atoms originally at the top of the cloud are now at the bottom, and vice versa.

Figure 9(b) shows the mean kinetic energy in the radial and the axial directions, E_ρ and E_z, for various ac trapping times within the same 61st switching cycle. The error bars indicate the standard deviations of the fit. The dashed lines correspond to the phases A–D of the switching cycle. As expected from Fig. 8, the velocities in the radial direction (squares) are higher than the velocities in the axial direction (circles) which is confirmed by our measurements. We also expect that the kinetic energy is minimal in the middle of the

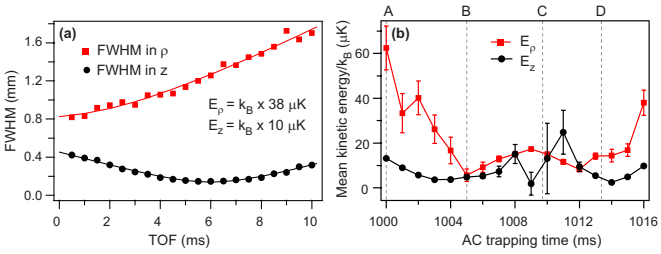

FIG. 9. (Color online) (a) Ballistic expansion measurements of the ac trapped cloud after a trapping time of 1016 ms at 60 Hz. Plotted are the measured FWHM of the cloud in the ρ (squares) and z (circles) directions versus the TOF. The solid lines show the corresponding fits. (b) Mean kinetic energies E_ρ (squares) and E_z (circles) of the atoms for various ac trapping times within the 61st switching cycle. The dashed lines indicate the times A–D in the switching cycle. All data points are plotted together with the associated error bars, which are the standard deviations of the fit.

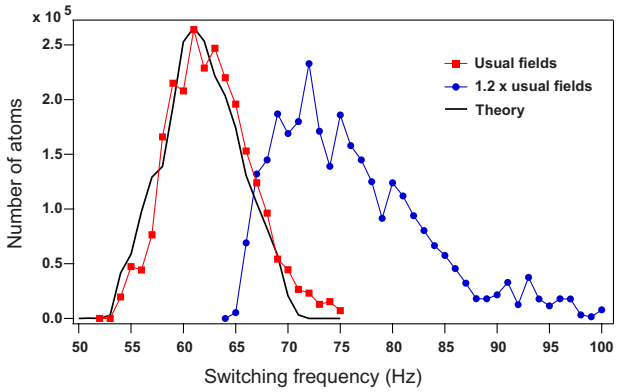

FIG. 10. (Color online) Frequency scan for two different sets of voltages. The squares show measurements where the voltages from Fig. 1 are employed. The solid curve is the corresponding theory prediction. The circles display measurements where higher voltages are used, resulting in electric fields that are 1.2 times stronger. The frequencies for stable trapping are then shifted to higher values. The number of atoms is measured after a trapping time of 5 s, and ten pictures are averaged for each data point.

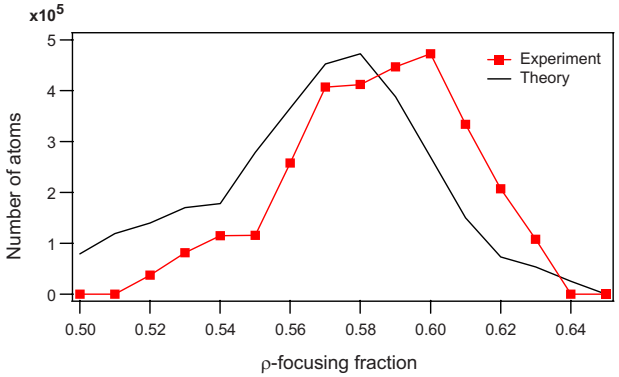

FIG. 11. (Color online) Atom number versus ρ-focusing fraction in a switching cycle of 16.7 ms corresponding to a switching frequency of 60 Hz. The data are taken after 1 s of trapping, and the measurements are averaged five times. The solid black curve is the simulation result.

focusing phases, i.e., at the turning points of the micromotion, B and D. Only at these phases of the switching cycle can we exclude the contribution of the micromotion to the kinetic energy. From measurements at point B and close to point D, we obtain minimum values of about $k_B \times 10$ μK for the mean kinetic energy.

As the atoms do not have well-defined Gaussian velocity distributions across the entire switching cycle, the FWHM fits of the expanding cloud can have large error bars. This is primarily the case for ac trapping times where the motion of the atoms is governed by the defocusing forces, i.e., from the middle of the defocusing phase to the middle of the next focusing phase. Therefore, as seen in Fig. 9(b), in the radial direction we obtain larger error bars for trapping times between D and B via A. Here we take into account the fact that the switching cycle wraps around, i.e., the end of one cycle coincides with the beginning of the next cycle. For the axial direction, the error bars are largest for trapping times between B and D, that is to say for the complementary part of the switching cycle.

Figure 10 shows the number of trapped atoms versus the applied switching frequency after a 5 s trapping time. Two different sets of voltages are used. The frequency scan plotted with squares was obtained using the voltages indicated in Fig. 1. For the measurement plotted with circles, the applied voltage set results in an electric field that is a factor of 1.2 higher. The solid curve is a simulation carried out using the lower-voltage set which is in excellent agreement with the experimental data. For the lower voltages, trapping works in a rather narrow range between 54 and 75 Hz with a maximum of 2.5×10^5 atoms trapped at 61 Hz after 5 s. No trapping is observed below the 54 Hz threshold. For the higher voltages, trapping occurs at higher switching frequencies, as expected. As with the lower voltages, there is a strong increase in signal above the threshold frequency of 64 Hz, and a slowly decreasing signal for the higher frequencies. Here, the range of working frequencies is broader. Despite the deeper trapping potential at higher voltages, the recorded number of trapped atoms is smaller, which we attribute to tiny discharges that we did not observe for the lower voltages. These discharges lead to a local increase in pressure which reduces the number of trapped atoms due to a higher rate of background collisions.

In Fig. 11 the relative switching time of ρ versus z focusing is varied, while the duration of the switching cycle is held constant at 16.7 ms. The first data point refers to a symmetric switching cycle with 50% of ρ focusing and 50% of z focusing, where no signal is observed. The number of trapped atoms increases with increasing ρ-focusing time. The maximum atom number after 1 s of trapping is 4.5×10^5 and is found for a switching cycle with 60% of ρ focusing. For longer ρ-focusing times the number of atoms quickly decreases with no signal observed from 64% onwards. The solid curve is the corresponding theory prediction and shows the same trend as the experimental data. There is a clear shift, however, between theory and experiment, with the theoretical maximum at a smaller value of the ρ-focusing fraction. The asymmetry of the switching cycle is partly explained by the need to compensate for differences between the ideal trapping geometry and the actual experimental configuration. The experimental misalignments are likely more complex than the already mentioned retracted end cap geometry, which is taken into account in our simulations.

VII. PROBING THE PHASE-SPACE ACCEPTANCE OF THE TRAP

The phase-space acceptance can be probed by introducing a sudden change in the switching cycle. Most of the atoms have the wrong initial conditions to survive this change and they will be lost from the trap. Only the few atoms that reside in the accepted part of the phase-space distribution will remain trapped if more switching cycles are applied afterward.

For this experiment, a truncated switching cycle is applied to the stably trapped atom cloud. We will refer to this modified switching cycle as a "phase jump." First, 60 switching

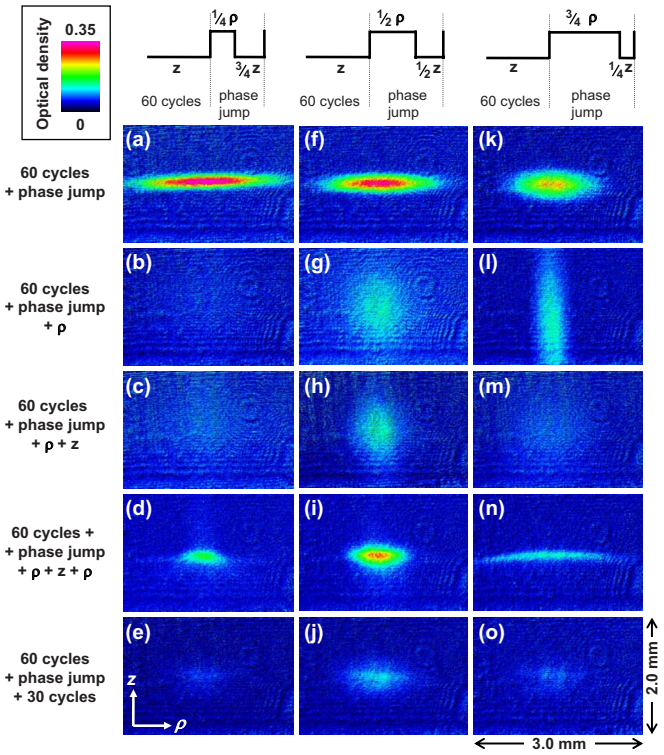

FIG. 12. (Color online) Pictures of the atom cloud after 60 switching cycles at 60 Hz followed by a phase jump. For the first column (a)–(e), ρ focusing is on for only 1/4 of its usual duration and z focusing is on for 3/4 of its usual setting. For the second column (f)–(j), a symmetric phase jump is performed with 1/2 ρ focusing and 1/2 z focusing. In the third column (k)–(o), 3/4 of ρ focusing is followed by 1/4 of z focusing. Each column shows the atoms imaged directly after the phase jump (first row), after an additional ρ-focusing phase applied after the phase jump (second row), after a full switching cycle applied after the phase jump (third row), after a full cycle and a ρ-focusing phase (fourth row), and when 30 full switching cycles have been applied after the phase jump (last row). All pictures are averaged five times.

cycles with the usual 59% of ρ focusing and switching frequency of 60 Hz are applied. This ensures that most of the metastably trapped atoms have escaped from the trap. Then comes a cycle with reduced durations for both the ρ- and the z-focusing phases. This is illustrated in Fig. 12. In the first column, a phase jump is applied where the ρ focusing is reduced to 1/4 and the z focusing is reduced to 3/4 of their usual durations. For the measurements in the second column, a symmetric phase jump is applied, i.e., a 1/2 ρ-focusing phase is followed by a 1/2 z-focusing phase. In the third column, the measurements are again taken for an asymmetric phase jump with 3/4 of ρ focusing and 1/4 of z focusing.

In the first row of Fig. 12, the cloud is imaged directly after the phase jump. From left to right, the radial extent of the cloud decreases while the cloud becomes larger in z. In Fig. 12(a) the atoms have been exposed to z focusing longer than to ρ focusing, which keeps the cloud tightly together in z, whereas the atoms spread out in ρ. In Fig. 12(k), due to the short z-focusing phase, the cloud is spread out in z and confined in ρ. In Fig. 12(f) the phase jump is symmetric and the cloud shape is intermediary between the situations in Figs. 12(a) and 12(k). The pictures in the second row show the atoms after the application of an additional, full ρ-focusing phase. As a consequence, from Fig. 12(b) via Fig. 12(g) to Fig. 12(l), the atoms are more focused in the ρ direction. In Fig. 12(b) the cloud density is very low making the atoms barely visible. In Fig. 12(g) the cloud is fairly well confined because the atoms are not as perturbed as in Figs. 12(b) and 12(l) due to the symmetric switching. In Fig. 12(l) the cloud is spreading out along z as it has experienced only a short z-focusing phase. In the third row a subsequent full z-focusing stage is applied so that the atoms have by now experienced one full switching cycle after the phase jump. In Fig. 12(c) the density has increased due to the z focusing, and a very dilute cloud is now visible. In Fig. 12(h) the cloud is pretty well confined. In Fig. 12(m) atoms have escaped from the trap along the z direction, the additional defocusing in ρ during the z-focusing phase leading to a dilute cloud. In the fourth row an additional ρ-focusing phase is applied. For both asymmetric phase jumps the atoms now form a small cloud. Very interesting is the pancake shape in Fig. 12(n), elongated along ρ and focused in z due to the prior phase of z focusing. Looking at the series in Figs. 12(l)–12(n), we notice that the cloud changes dramatically, being ρ focused in Fig. 12(l) and dilute in Fig. 12(m) because of the reshaping. The last row shows the atoms after 30 full switching cycles have followed the phase jump. For the asymmetric switching procedures in Figs. 12(e) and 12(o) few atoms survive, whereas in the case of symmetric switching more atoms remain confined in the trap.

As discussed for Fig. 8, the trap acceptance varies with the phase in the switching cycle. To visualize how the motion of the trapped atoms is perturbed by the symmetric phase jump (i.e., 1/2 ρ focusing followed by 1/2 z focusing), we carried out simulations which include the phase jump and the subsequently applied 30 full switching cycles. Note that only the atoms that survive these final 30 cycles will be discussed in the following. If this truncated switching cycle is applied, the distribution and therefore the phase space acceptance in the middle of ρ focusing is mapped onto the distribution in the middle of z focusing. This happens because the second half of ρ focusing and the first half of z focusing are missing in the modified cycle. Figure 13 shows the calculated phase-space distributions, where v_z is displayed versus z. The phase-space distribution after the ρ-focusing stage of the phase jump is presented in Fig. 13(a), along with the distributions already shown in plots B and D of Fig. 8. Only those atoms that are in a region of phase space where the distribution after 1/2 ρ focusing (black) overlaps with the distribution after 1/2 z focusing [dark gray (magenta online)] will remain trapped. Therefore, after the ρ-focusing stage of the phase jump the accepted phase space has reduced to this overlap region [light gray (orange online)]. In Fig. 13(b), this reduced distribution is again illustrated, along with the distributions after the entire phase jump [black (blue online), corresponding to Fig. 12(f)] and after an additional ρ-focusing stage [dark gray (red online), corresponding to Fig. 12(g)]. At the end of the phase jump and therefore at the beginning of the next switching cycle, the distribution has rotated clockwise by 45°, as we expect from plot A in Fig. 8. While this distribution is narrow in both velocity and posi-

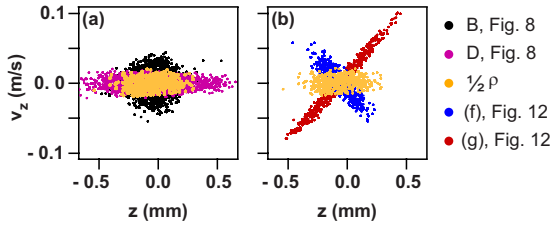

FIG. 13. (Color online) Simulated phase-space distributions where v_z is plotted versus z. The figures show those atoms that survive the symmetric phase jump and the subsequently applied 30 full switching cycles. In (a), the phase-space distribution after the ρ-focusing stage of the phase jump [light gray (orange online)] is plotted, along with the distributions already shown in plots B (black and D [dark gray (magenta online)] of Fig. 8. In (b), this distribution [light gray (orange online)] is shown again, along with the distributions after the entire phase jump [black (blue online), corresponding to Fig. 12(f)], and after an additional ρ-focusing stage [dark gray (red online), corresponding to Fig. 12(g)].

tion, the distribution after an additional ρ-focusing stage starts to spread out, thereby gradually refilling the whole accepted area in phase space.

It becomes clear from these simulations and the associated measurements that the overlap of the accepted areas in phase space is optimal for a symmetric phase jump. For asymmetric phase jumps, more atoms are located in the unaccepted region of phase space and will therefore be lost from the trap. This is also visible in the last row of Fig. 12.

VIII. CONCLUSIONS

In this paper, we have presented a detailed study on trapping of rubidium in an ac electric trap. First, we showed that the atoms can be used to probe the electric fields in the trap, and we reproduced our results with simulations. By studying the gradual formation of a trapped cloud, we observed that most of the atoms that are not stably confined leave the trap within the first second. In a typical experiment, 3×10^5 atoms are stably trapped with a lifetime of about 9 s, limited by collisions with the background gas. One of the nice features of our ac trap is the ability to directly visualize the atom dynamics at different phases of the switching cycle using absorption imaging. Trajectory calculations were carried out to confirm this dynamic behavior and to understand the corresponding phase-space distributions. Additionally, the mean kinetic energy of the trapped cloud was observed to vary across the switching cycle, as it is dominated by the micromotion in the trap. Values of about 10 μK were measured at the points where the micromotion does not contribute. We have also studied the dependence of the trapped atom number on the switching frequency and the symmetry of the switching cycle. Stable trapping occurs for a narrow frequency range around 60 Hz and for an asymmetric switching cycle. Finally, when a modified switching cycle is applied, the motion of the atoms in the ac trap can be readily understood from simulations of the phase-space acceptance at various phases of the switching cycle.

ACKNOWLEDGMENTS

This work is part of the research program of the "Stichting voor Fundamenteel Onderzoek der Materie (FOM)," which is financially supported by the "Nederlandse Organisatie voor Wetenschappelijk Onderzoek (NWO)." A.M. would like to thank the Alexander von Humboldt Foundation for their support. We acknowledge useful discussions with Sam Meek, Allard Mosk, Achim Peters, and Boris Sartakov, and technical assistance from Peter Geng.

[1] M. H. Anderson, J. R. Ensher, M. R. Matthews, C. E. Wieman, and E. A. Cornell, Science **269**, 198 (1995).
[2] B. DeMarco and D. S. Jin, Science **285**, 1703 (1999).
[3] M. Lara, J. L. Bohn, D. Potter, P. Soldan, and J. M. Hutson, Phys. Rev. Lett. **97**, 183201 (2006).
[4] W. H. Wing, Prog. Quantum Electron. **8**, 181 (1984).
[5] W. Ketterle and D. E. Pritchard, Appl. Phys. B **B54**, 403 (1992).
[6] R. Grimm, M. Weidemüller, and Y. B. Ovchinnikov, Adv. At., Mol., Opt. Phys. **42**, 95 (2000).
[7] S. Chu, J. E. Bjorkholm, A. Ashkin, and A. Cable, Phys. Rev. Lett. **57**, 314 (1986).
[8] T. Takekoshi, B. M. Patterson, and R. J. Knize, Phys. Rev. Lett. **81**, 5105 (1998).
[9] E. A. Cornell, C. Monroe, and C. E. Wieman, Phys. Rev. Lett. **67**, 2439 (1991).
[10] W. Paul, Rev. Mod. Phys. **62**, 531 (1990).
[11] J. van Veldhoven, H. L. Bethlem, and G. Meijer, Phys. Rev. Lett. **94**, 083001 (2005).
[12] M. Schnell, P. Lützow, J. van Veldhoven, H. L. Bethlem, J. Küpper, B. Friedrich, M. Schleier-Smith, H. Haak, and G. Meijer, J. Phys. Chem. A **111**, 7411 (2007).
[13] T. Kishimoto, H. Hachisu, J. Fujiki, K. Nagato, M. Yasuda, and H. Katori, Phys. Rev. Lett. **96**, 123001 (2006).
[14] S. Schlunk, A. Marian, P. Geng, A. P. Mosk, G. Meijer, and W. Schöllkopf, Phys. Rev. Lett. **98**, 223002 (2007).
[15] E. Peik, Eur. Phys. J. D **6**, 179 (1999).
[16] T. Rieger, P. Windpassinger, S. A. Rangwala, G. Rempe, and P. W. H. Pinkse, Phys. Rev. Lett. **99**, 063001 (2007).
[17] F. Shimizu and M. Morinaga, Jpn. J. Appl. Phys., Part 2 **31**, L1721 (1992).
[18] M. Morinaga and F. Shimizu, Laser Phys. **4**, 412 (1994).
[19] H. L. Bethlem, J. van Veldhoven, M. Schnell, and G. Meijer, Phys. Rev. A **74**, 063403 (2006).
[20] H. J. Lewandowski, D. M. Harber, D. L. Whitaker, and E. A. Cornell, J. Low Temp. Phys. **132**, 309 (2003).
[21] C. Krenn, Z. Phys. D **41**, 229 (1997).